Journal of Applied Fluid Mechanics, Vol. 16, No. 8, pp. 1500-1514, 2023.
Available online at www.jafmonline.net, ISSN 1735-3572, EISSN 1735-3645.
https://doi.org/10.47176/jafm.16.08.1707

Development of an Intelligent Passive Device Generator for Road Vehicle Applications

R. Aranha, N. A. Siddiqui†, W. Y. Pao and M. Agelin-Chaab

Faculty of Engineering and Applied Science, Ontario Tech University, Oshawa, Ontario, L1G0C5, Canada

†*Corresponding Author Email: naseeb.siddiqui@ontariotechu.net*

ABSTRACT

Flow control has a tremendous technological and economic impact, such as aerodynamic drag reduction on road vehicles which translates directly into fuel savings, with a consequent reduction in greenhouse gas emissions and operating costs. In recent years, machine learning has also been used to develop new approaches to flow control in place of more laborious methods, such as parametric studies, to find optimal parameters with few exceptions. This paper proposes an intelligent passive device generator (IPDG) that combines computational fluid dynamics (CFD) and genetic algorithm, more specifically, the Non-dominated Sorting Genetic Algorithm II (NSGA II). The IPDG is not application specific and can be applied to generate various devices in the given design space. In particular, it creates three-dimensional passive flow control devices with unique shapes that are aerodynamically efficient in terms of the cost function (i.e., aerodynamic drag and lift). In this paper, the IPDG is demonstrated using a rear flap and an underbody diffuser as passive devices. The three-dimensional Reynolds-averaged Navier-stokes (RANS) equations were used to solve the problem. Relative to the baseline, the IPDG generated flap-only, and diffuser-only provide drag reductions of 6.3% and 5.4%, respectively, whereas the flap-diffuser combination provides a drag reduction of 7.4%. Furthermore, the increase in the downforce is significant from 624.4% in flap-only to 4930% and 4595% in the diffuser and flap-diffuser combination. The proposed method has the potential to evolve into a universal passive device generator with the integration of machine learning.

Article History

Received December 10, 2022
Revised April 7, 2023
Accepted April 9, 2023
Available online May 31, 2023

Keywords:

Machine learning
Flow control
Shape optimization
Genetic algorithm
Drag reduction

1. INTRODUCTION

In the last ten years, there has been renewed interest in the study of how to regulate turbulent flows, in particular for the aim of lowering drag (Noack, 2019). The control of wake flows has sparked considerable interest due to its importance in a wide range of applications. The flow control tactics frequently focus on drag reduction (DR) along with the control of lift, downforce, soiling, and stability of the road vehicle in question. The development of effective flow control strategies is a difficult goal, particularly when the answer is based solely on restricted velocity or pressure data retrieved from the fluid flow (Duriez et al., 2013). The flow control problem is, at heart, a functional optimization problem wherein the state of the dynamical system must be inferred from a small set of measured variables. The goal is to identify a control function for the regulated flow configuration that reduces a cost function. In the context of classifying control techniques, distinguishing between model-based and model-free control is a key distinction. In the latter, a model of the dynamical system is not imposed in order to derive an optimal control law. Recent years have seen a meteoric rise in the use of such methods, mostly due to the widespread adoption and development of machine learning strategies. One of the popular methods reported in the machine-learning literature is evolutionary algorithms. They are concentrated on recombining effective control policies by testing, leveraging the ones that produce the greatest outcomes, and looking into potential alternatives in the solution space (Goldberg & Holland, 1988; Koza, 1994).

Nomenclature

IPDG	Machine learning inspired intelligent passive device generator	RANS	Reynolds-Averaged Navier-Stokes Equations
t	Knot parameters	PFC	Passive Flow Control
t’	Surface thickness		

Flow control devices are broadly categorized into active and passive. Several active devices have been used in the literature, including movable underbody diffusers, steady blowing, steady suction, plasma actuators, and synthetic jets (Yu & Bingfu, 2021). However, active devices require external energy and electronics to function. Due to such difficulties, the technologies are not yet mature enough to handle the dynamics involved. On the other hand, passive devices provide comparable DR and are easy to implement without any extra energy and work as add-on devices which makes their operation simple. According to the literature, compared to the other passive devices, flaps provide better DR. For instance, Beaudoin and Aider (2008) obtained a DR of 25% from their modified Ahmed body with small rectangular flaps at the edges. Such a mechanism made the flow fully separate at the slant and reduced the C-vortex emanating from the side edges. Also, Fourrié et al. (2011) employed a curved deflector on a 25° slant Ahmed body and obtained a DR of 9% by modification of the C-vortex. Additionally, the study reported by Tian et al. (2017) examined the benefits of flaps used on 25° and 35° slant Ahmed bodies. They reported DR of 21.2% and 6% for the 25° and 35° Ahmed models, respectively. Building on the works of Beaudoin and Aider (2008) and Fourrié et al. (2011), Hanfeng et al. (2016) implemented a flap at the side edges and the top edge of the slant surface over a 25° Ahmed body. Their investigation achieved 11.8% DR is much smaller than the previous works.

In the area of flow control, machine learning has been applied to active flow control (AFC) cases. For example, in order to control actuators using input gathered by sensors in the step flow problem, Gautier et al. (2015) used genetic programming. Also, Zhou et al. (2020) employed genetic programming to create a real-time artificial intelligence control system to maximize the mixing rate of turbulent jets by searching for an unsupervised learning technique that is close to the optimal control law. It is impossible to directly deduce the turbulence theory due to the complexity of the turbulence problem, however, the development of deep neural networks is making this possible by leveraging massive datasets. The anticipated outcomes were attained using a deep neural network to learn the link between wall shear stress and actuator control (Lee et al., 1997). The transonic buffet flow was the subject of numerically applied data-driven adaptive control using the radial basis function neural network, where the trailing edge flap served as the actuator and the lift served as the feedback signal (Ren et al., 2020). Their flow control method significantly reduced the buffeting load. For DR, Li et al. (2017) installed pulsed Coanda jets at the four trailing edges of the square-back Ahmed body. By optimizing the cost function based on the base pressure signal, linear genetic programming (LGP) was used to determine the appropriate control settings, producing a maximum DR of 24%. To reduce drag on a slanted Ahmed body at 35º, a recent numerical study found that constant blowing along all edges of the back window and the base resulted in a DR of 17% with inward blowing. The strength and angle of all the blowing jets were optimized with the use of a revolutionary explorative gradient method (EGM) (Li et al., 2022). This strategy alternates between the downhill simplex method (DSM) and the Latin hypercube sampling technique. The DSM algorithm, in contrast to the gradient-based search algorithm, descends to a local minimum using just knowledge of its immediate surroundings (Nelder & Mead, 1965). This EGM method is used experimentally as well (Fan et al., 2020).

Within machine learning flow control methods, the model-free genetic algorithm has found special attention in the literature due to its non-gradient-based approach. They are a subset of evolutionary algorithms, which share a common workaround. A generation of individuals competes at a given task with a well-defined cost function and evolves based on rules, promoting successful strategies to the next generation (Banzhaf et al., 1998). It is a potent regression technique that can, without physics knowledge, rediscover and combine flow control strategies that have been shown to be effective in autoregressive moving average eXogenous (Maceda et al., 2019, 2021). Tree-based genetic programming has been used to develop laws ranging in complexity from phasor control to jet mixing optimization (Zhou et al., 2020), unsteady minijet for control (Wu et al., 2018), flow separation control (Gautier et al., 2015), vortex induced vibrations (Ren et al., 2019), and wake stabilization (Raibaudo et al., 2020). The machine learning flow control framework has undergone some necessary revisions, such as the adoption of an LGP algorithm, which is the path taken for the purposes of this investigation.

Furthermore, Shape optimization with genetic algorithms has been used in a number of aerodynamic-related applications. Muñoz-Paniagua and García (2020) optimized the train nose using Bezier Curves with one objective function for DR, the genetic algorithm was combined with a neural network to speed up the process. Both Yu et al. (2013) and Yuan and Li (2017) used script files that contained more than 160 control points to generate the train nose, a few of those points were chosen to be design variables to be optimized for drag and load reduction and drag and noise reduction. The elitist Nondominated Sorting Genetic Algorithm II (NSGA-II) was used, which is different from the standard genetic algorithm. The NSGA-II is not based on probability and can handle multiple

objectives, which ensures that all the best solutions are kept. For example, Yu et al. (2013) used NSGA-II algorithm to optimize the high-speed train head, which reduced drag by 4.2% and load reduction factor by 1.7%. Similarly, Yuan and Li (2017) employed an improved NSGA-II to optimize the aerodynamic drag and noise of the high-speed train. This improved NSGA-II algorithm takes a back propagation neural network model as the optimization evaluation system. Such an optimization method reduced the high-speed train drag by 6.7% and dipole aerodynamic noise by 8.3 dB. However, only a few researchers have employed genetic algorithms to optimize passive devices. Muyl et al. (2004) used a hybrid genetic algorithm to optimize the boat tail to reduce drag by varying the angle. Their results showed that the hybrid algorithm is more effective in both DR and computational time compared to the standard genetic algorithm. Similarly, Doyle et al. (2008) used a standard genetic algorithm to optimize rear flaps for trucks. Their simple two-dimensional (2D) study achieved 50% DR. However, three-dimensional (3D) bluff body flows were not considered.

Since the application of passive flow control (PFC) devices have demonstrated tremendous aerodynamic benefits in terms of drag and downforce, their importance cannot be ignored (Yu & Bingfu, 2021). For PFC, the methods developed so far are few, application-oriented and cannot be generalized. Furthermore, a method that can generate three-dimensional PFC devices for road vehicles based on the given design space and cost function using genetic algorithms is not reported in the open literature as far as the authors are aware, with the only exception being the work of Muyl et al. (2004). Moreover, future PFC devices should provide unique and non-intuitive shapes that could fit into the brand-differencing of road vehicle manufacturers and can easily align with future non-conventional vehicle shapes.

The use of machine learning on the Ahmed body has been recently highlighted in the literature review conducted by Yu and Bingfu (2021). Machine learning has found application in the Ahmed body using active flow control devices. Whereas the optimization of the passive flow control has not gained considerable attention. Therefore, the present investigation is well situated in the gap to develop PFC methods based on the genetic algorithm which represents machine learning. The developed method is called the intelligent passive device generator (IPDG). In this paper, the IPDG is demonstrated using the flap and diffuser as a passive device optimization. The following sections describe the IPDG method in detail.

2. FORMULATION OF IPDG

The proposed IPDG consists of the NSGA-II since it can optimize multiple objective functions. Several previous works have shown its efficiency and applicability (Liu et al., 2017). This method can generate complex surfaces, such as three-dimensional B-splines surfaces, based on the

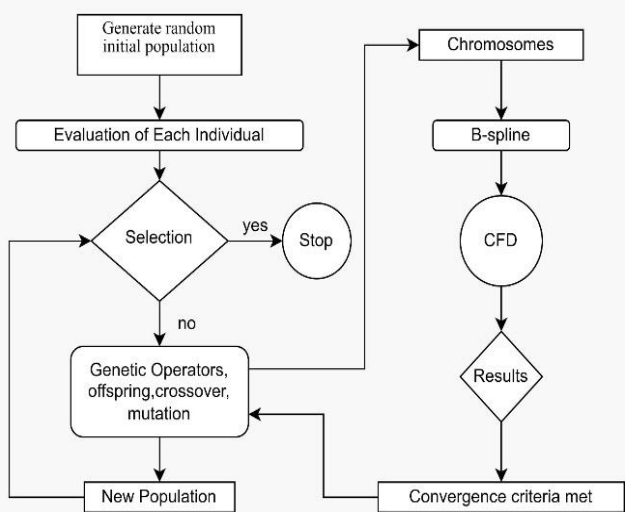

Fig 1. Intelligent passive device generator optimization flow chart.

background work and by Deb et al. (2002). The NSGA-II algorithm selects solutions based on dominance (ranking) and crowding distance. For example, if an individual outperforms others in all the objective functions, it will be ranked higher. The front f^m is assigned to individuals with the same rank, and the selection will prioritize individuals on better fronts. The crowded distance will take place in the case of ties (selection of some individuals in the same front). This process is called crowded tournament selection. The crowded distance calculation is expressed as:

$$d_i = d_i + \frac{f_{i+1}^m - f_{i-1}^m}{f_1^m - f_N^m} \quad (1)$$

Where i, m, N represent the individual, the front in which that individual belongs, and the population size, respectively.

2.1 Implementing the NSGA-II

Figure 1 shows the integration of NSGA-II, and B-spline with OpenFOAM in the optimization process, which is divided into two parts. The left column shows the algorithm sequence and the right column displays the evaluation of individuals within the population. The whole algorithm (left column) begins by generating the random population size. Next, an evaluation takes place to import the objective functions. For this demonstration, the objective functions are the drag and lift. When the optimization begins (right column), it generates a population such that every individual has a unique chromosome which is then translated into a B-spline surface through a user-defined procedure in MATLAB. This surface is then exported into an STL file format for the computational fluid dynamics (CFD) analysis. After the evaluation, the action of the genetic operators, namely, crossover and mutation, will begin and generate a new population, which is also then subjected to the next round of evaluations, and the process continues until the convergence criteria are met. In all the scenarios considered

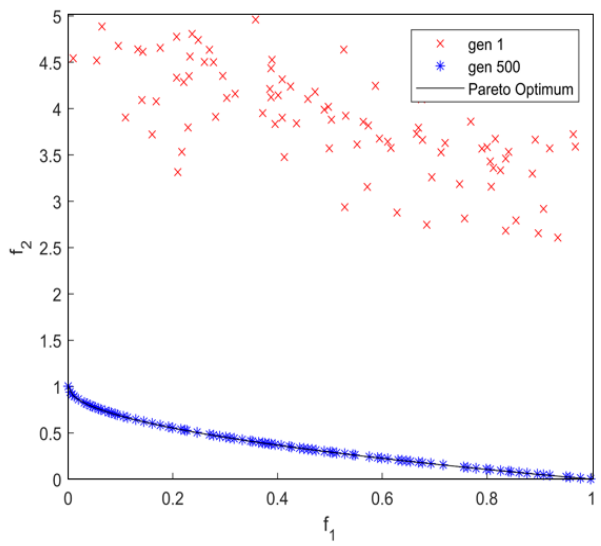

Fig. 2. NSGA-II benchmarking for 1st and 500th generations and comparison with the Pareto Optimum results.

in this study, the method implemented runs for the same time span, starting with random genes. In this way, the number of generations achieved depends on the computational cost of an individual run. In the end, the method was able to reach 15-18 generations with a population size of 20. It was observed that there are significant differences between the individuals in the 1st generation and those of the 15th -18th generations, showing the evolution from generation to generation. For better results, the method should be allowed to run for several generations. However, due to limited computational resources, it could only achieve 15-18 generations in the present study. Nonetheless, the number of generations is sufficient to evaluate the performance of the method developed in this study. It should be noted that for a single run of the method, several unique geometries can be generated, up to 70 geometries. More importantly, each of the geometries is optimized based on the specified objectives, in this case, drag and lift reduction.

2.2 Benchmarking

A benchmark function with a known solution was used to test the algorithm prior to the OpenFOAM CFD simulation. The function selected was the ZDT1 function; the benchmark equations are well-known and can be found in Yang (2013).

The NSGA-II parameters are as follows: the population size, mutation probabilities, and crossover were 20, 5%, and 85%, respectively. These parameters were selected based on the optimization algorithm testing, where the probabilities are in the acceptable range, according to Hassanat et al. (2019). Figure 2 shows that the NSGA-II algorithm converged to the known solution after 500 generations with 7 bits of precision and 3-dimensional variables ranging from zero to one.

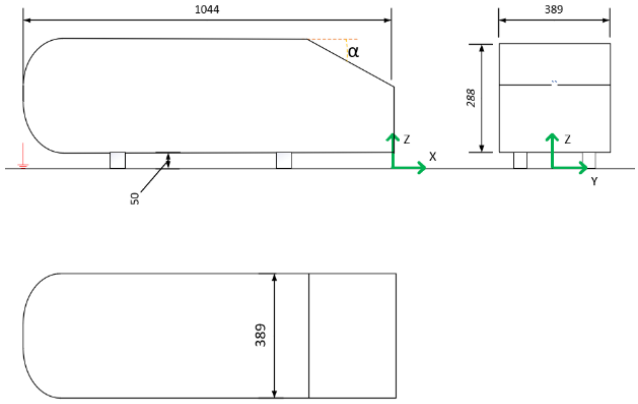

Fig. 3. The Ahmed body dimensions (mm), where α is the slant angle (Ahmed et al., 1984).

3. GEOMETRY GENERATION

The flow around the Ahmed body with a slant angle of 35° is well understood, and hence the new IPDG method is applied to control its aerodynamic drag and lift. Figure 3 presents the dimensions of the Ahmed body (Ahmed et al., 1984), where the length is 1044 mm, width is 389 mm, and height is 288 mm.

The flap and diffuser represented the PFC and were generated using the user-defined MATLAB B-Spline function. It is emphasized that the flap is a standard add-on device, whereas the diffuser in this study is a cut-out piece from the bottom of the rear end, and both are free to develop in the design space producing unique shapes. The B-spline surfaces of order k were generated from a linear combination of k-1 polynomials and continuity C^{k-2} over the control points P (Patrikalakis & Maekawa, 2010). The knot basis curves were generated based on breakpoints, with the knot vector T = (t_0, t_1, …t_m) using Eqs. (2-4), where t is a knot parameter for a linear combination between the points on the surface:

$$N_{i,1}(t) = \{1 \ for \ t_i \leq t < t_{i+1} \ 0\} \ otherwise \tag{2}$$

$$N_{i,k}(t) = \frac{t - t_i}{t_{i+k-1} - t_i} N_{i,k-1}(t) + \frac{t_{i+k} - t}{t_{i+k} - t_{i+1}} N_{i+1,k-1}(t) \tag{3}$$

$$r(u,v) = \sum_{i=0}^{m} \sum_{j=0}^{n} p_{ij} N_{i,k}(u) N_{j,l}(v) \tag{4}$$

A uniform knot vector (0, 1) was used to improve the accuracy and simplify the meshing of the STL files while generating the base curves $N_{i,k}(t)$. Repeating the breakpoints by k will ensure the curves end at the last point suggested by Patrikalakis and Maekawa (2010), which allows the control of the beginning and completion of the surface. The number of points in the knot vector is *2k+n+1*,

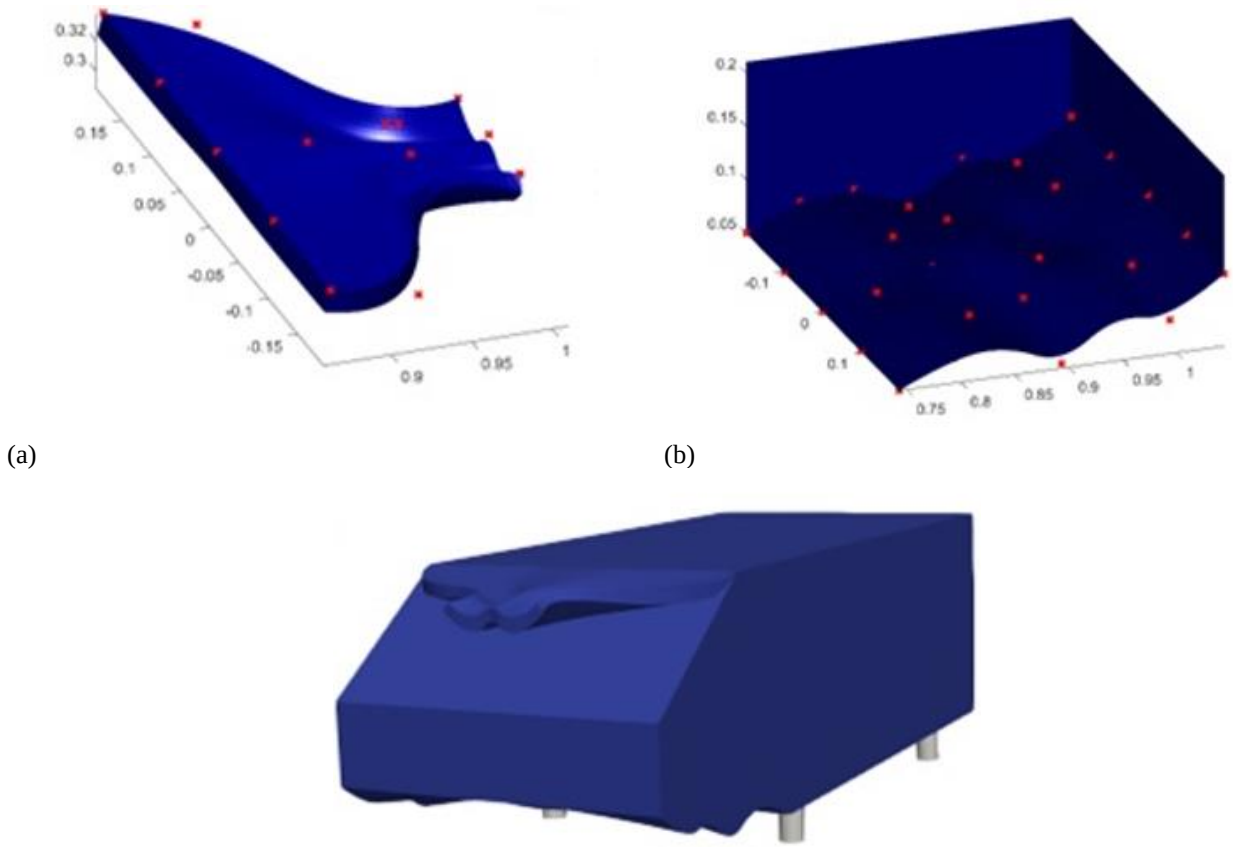

(a) (b)

(c)

Fig. 4. Illustration of surface generation from control points for: (a) flap, (b) diffuser; control points are indicated in red crosses, and (c) Integration of the devices with unique surfaces to the Ahmed body; the assembly models were exported to OpenFOAM for CFD analysis.

where *k* and *n+1* denote the B-Spline order and number of control points, respectively. The genetic algorithm has been applied to the positions of the control points. Yet, with different sets of control points, it was possible to generate a variety of curves of order 3.

Furthermore, a gradient technique was used to extrude the surfaces and the orthogonal vector to calculate the partial differential at each point of the surfaces to generate the gradient, as shown in equation (5). Here *G* is the gradient of the function *F(x,y)*, and *t'* is the thickness of the surface. Equation (7) was used to calculate the first-order finite difference, which showed a minor error. Figure 4 displays the control points on the devices and the full assembly of the flap and diffuser over the Ahmed body.

$$\left(x_{i_2}, y_{j_2}, F_{ij_2}\right) = \left(x_i, y_j, F_{ij}\right) + G_{ij}.\, t'/\|G_{ij}\| \tag{5}$$

$$G_{ij} = \left(F_{ij_x}, F_{ij_y}, -1\right) \tag{6}$$

$$F_{ij_x} = \frac{F_{ij} - F_{i-1,j}}{x_i - x_{i-1}} \tag{7}$$

4. NUMERICAL MODEL

4.1 Governing Equations and Boundary Conditions

The steady-state RANS equations for mass and momentum are:

Continuity

$$\frac{\partial}{\partial x_i}\left(\overline{\rho u_i}\right) = 0 \tag{8}$$

Momentum

$$\begin{aligned}\frac{\partial}{\partial x_j}\left(\overline{\rho u_i u_j}\right) = &-\frac{\partial \bar{p}}{\partial x_i} \\ &+ \frac{\partial}{\partial x_j}\left[\mu\left(\frac{\partial \overline{u_i}}{\partial x_j} + \frac{\partial \overline{u_j}}{\partial x_i} - \frac{2}{3}\partial_{ij}\frac{\partial \overline{u_l}}{\partial x_l}\right)\right] \\ &+ \frac{\partial}{\partial x_j}\left(-\rho\overline{u_i' u_j'}\right)\end{aligned} \tag{9}$$

Here $\bar{\rho}$ is the mean density, $\bar{p}$ is the mean pressure, μ the molecular viscosity and $-\rho\overline{u_i' u_j'}$ are the Reynolds stresses.

The equations are in the averaged form, and the closure terms are in equation (9) must be modelled. The term $-\rho\overline{u_i'u_j'}$ is the Reynolds tensor with nine components. This problem is known as the closure problem, and it is tackled by applying turbulence modelling.

Reynolds averaged Navier-Stokes (RANS) *k-ω* SST turbulence modeling was used to enhance the CFD simulations. Several studies have demonstrated that RANS with *k-ω* SST accurately captures the flow features around the 35º slant angle Ahmed body (Guilmineau, 2008). Since the 35° slanted Ahmed body model generates quasi axis-symmetric flow behaviour, the prediction of the flow behaviours is accurate. The same line of argument was made by Tian et al. (2017). The turbulence model was selected with considerations of cost and time required for the number of unique assemblies to be evaluated. However, sub-grid scale modeling is recommended to predict the flow behavior better when there is additional complexity on the bluff body, which causes flow separations.

The problem with setting up a simulation in OpenFOAM is how to handle the boundaries and the schemes correctly. To properly set up the boundary conditions in the inlet, the ANSYS user manual (Ansys, 2018) was used to copy the inlet function and use it in OpenFoam. The boundary conditions are set up with Eqs. (10-12), where κ is the turbulent kinetic energy, ω is a specific rate of dissipation, U is the inlet velocity, I is turbulent intensity and ν_r is viscosity ratio; and the input values for I, ν_r, and U are 0.25%, 10, and 40 m/s, respectively, whereas ν_t is calculated from the solution. The model height-based Reynolds number is nearly 7.6×10^5. The input values are based on Lienhart et al. (2002) wind tunnel experiments, with which the CFD has been validated.

$$\kappa = \frac{3}{2}(U \cdot I)^2 \tag{10}$$

$$\omega = \frac{\kappa}{\nu \cdot \nu_r} \tag{11}$$

$$\nu_r = \frac{\nu_t}{\nu} \tag{12}$$

4.2 Meshing

The model was meshed with the Snappy hex mesh, which is the standard mesh generation tool in OpenFOAM. It was then placed in an enclosure with dimensions of 3 m in length, 0.5 m in height, and 1 m in width. The quality of the mesh was controlled by non-orthogonality below 55 degrees such that it agrees well with the finite volume schemes restrictions, and y^+ is less than 5 or between 30-200 to be acceptable for the wall functions. The maximum element sizes were set to be 0.05 m at free stream regions and 0.00625 m at the refined region near the Ahmed body. The mesh was programmed to be automatic and include the geometries generated by the B-spline surfaces. The program also automatically processes the changes in geometries, which may include or exclude the new devices throughout the algorithm. Figure 5 shows the mesh of the symmetry-model Ahmed body with 35º slant angle.

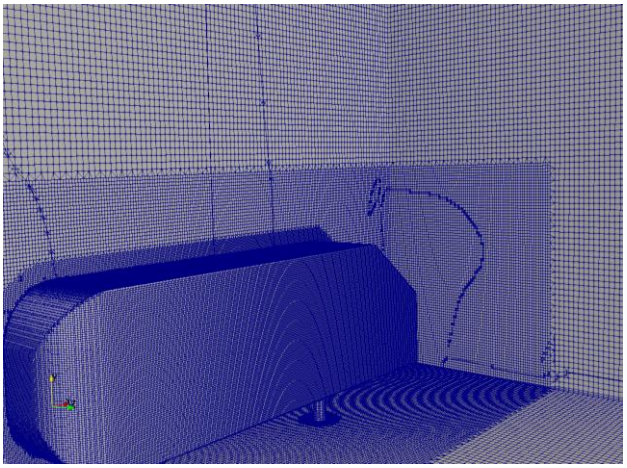

Fig. 5. Mesh of the Ahmed body with 35º slant angle.

A grid independence study was performed to check the sensitivity of the mesh on the flow. Figure 6 shows that results are independent of grid size, starting at about 1.0×10^7 elements, after which there was less than a 5% difference when compared with experimental results for an Ahmed body with a 35° slant angle (Lienhart et al., 2002). It was decided to use a grid size of around 1.5×10^7elements in order to have a fast and accurate simulation.

4.3. Validation of CFD Model

The CFD model in this study was validated with open-source experimental data and literature work (Ahmed et al., 1984; Lienhart et al., 2002; Meile et al., 2012; Tian et al., 2017). Figure 7 shows good agreements between the numerical results and experimental work reported by Lienhart et al. (2002) for the Ahmed Body with a 35º slant

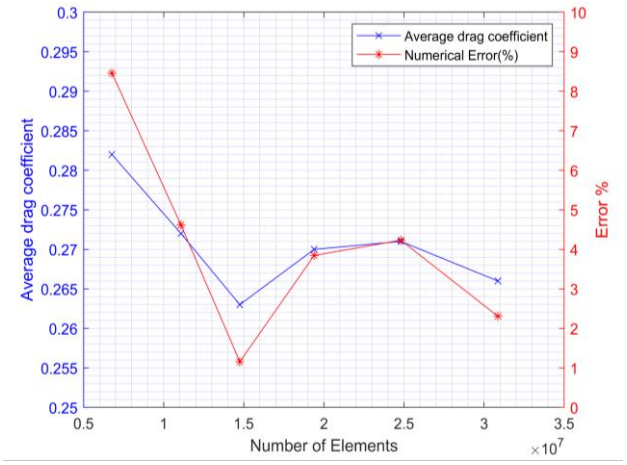

Fig. 6. Grid independence test and comparison of numerical and experimental errors.

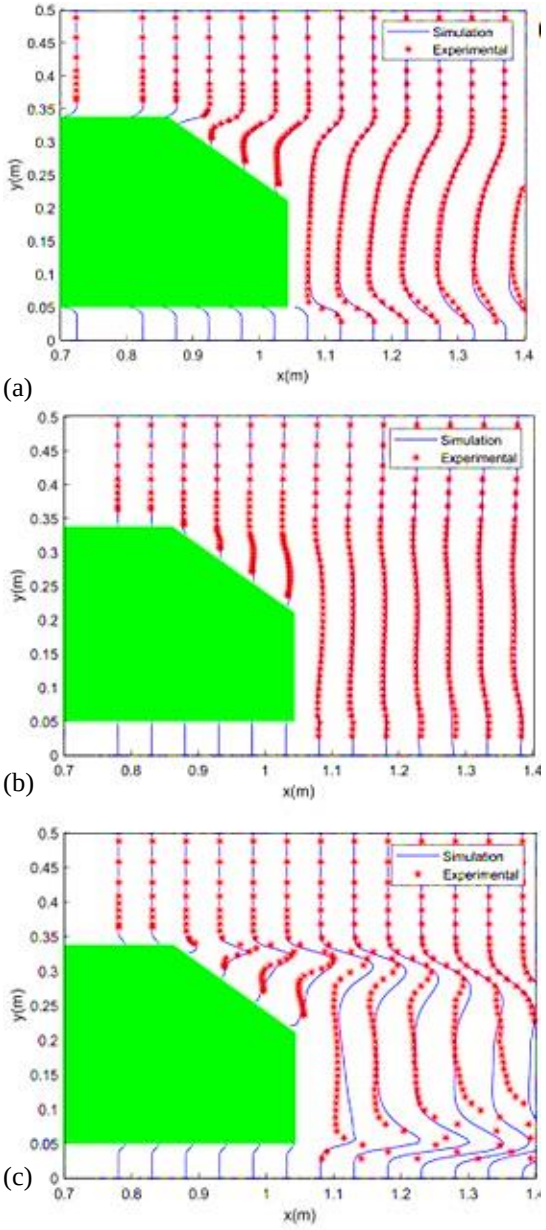

Fig. 7. Comparison of experimental data and simulation results. (a) Streamwise mean velocity, (b) mean transverse velocity, and (c) turbulence kinetic energy profiles.

Table 1 Experimental vs. present numerical study. Here, R. L. is the Recirculation length (the lift is in the Z direction)

Coefficient	**Experimental** (literature)	**Numerical** (present study)
C_d	0.26 (Ahmed et al., 1984)	0.2629
C_l	0.004 (Tian et al., 2017)	0.0082
R.L	1.2*h* (Siddiqui & Agelin-Chaab, 2021)	1.22h

angle on the streamwise and mean transverse velocities, as well as turbulence kinetic energy. Table 1 shows the comparison of the drag and lifts coefficients between the numerical results (present study) and experimental data from wind tunnels (Ahmed et al., 1984; Lienhart et al., 2002; Meile et al., 2012; Tian et al., 2017). The simulation model was set up with the same parameters as the wind tunnel test conditions.

5. RESULT AND DISCUSSIONS

5.1. Implementation of the Optimization Method

For the purpose of this paper, three PFC devices were examined, namely flap device only (flap-only), diffuser device only (diffuser-only), and combined flap and diffuser. All scenarios begin with random chromosomes/genetic information and run for the same time span. The computational cost of each individual member of the population limited the number of generations achieved. In this paper, a range of 15-18 generations with a population size of 20 was achieved. Figure 8 illustrates the progression of the drag and lift improvements in each generation. The lesser the drag and lift coefficients, the closer they are to optimal. From Fig. 8, the drag and lift reductions were observed as the generations progressed, and the latest generation improved significantly when compared to the first generation.

5.2 Examples of the Unique Device Geometries

As mentioned before that the NSGA-II is designed to generate unique geometries which cannot be created using parametric study. The NSGA-II generates non-conventional and non-intuitive PFC devices that depend on design space and the objective functions. The example geometries presented in Fig. 9 are the ones that have survived the competition and evolved to the latest generation.

5.3 Drag and Lift

All three cases were compared with the baseline model, which is the Ahmed body without the PFC devices. The unique geometries with the least drag in each optimization scenario were selected for detailed analysis of the CFD results to obtain physical insights. The drag and lift coefficients for the baseline and the optimized models are listed in Table 2. Their geometries are also displayed in Fig. 10(a)-(d).

5.4 Pressure Analysis

Figure 11 shows 2D images of pressure contours on the baseline and optimized models with the flap-only, diffuser-only, and combined flap-diffuser to show the effects of the aerodynamic devices developed. For the flap-only model in Fig. 11(b), it can be observed that pressure at the rear increased when compared to the baseline model causing a DR. This is evident from a lower pressure region at the rear of the baseline case in Fig. 11(a).

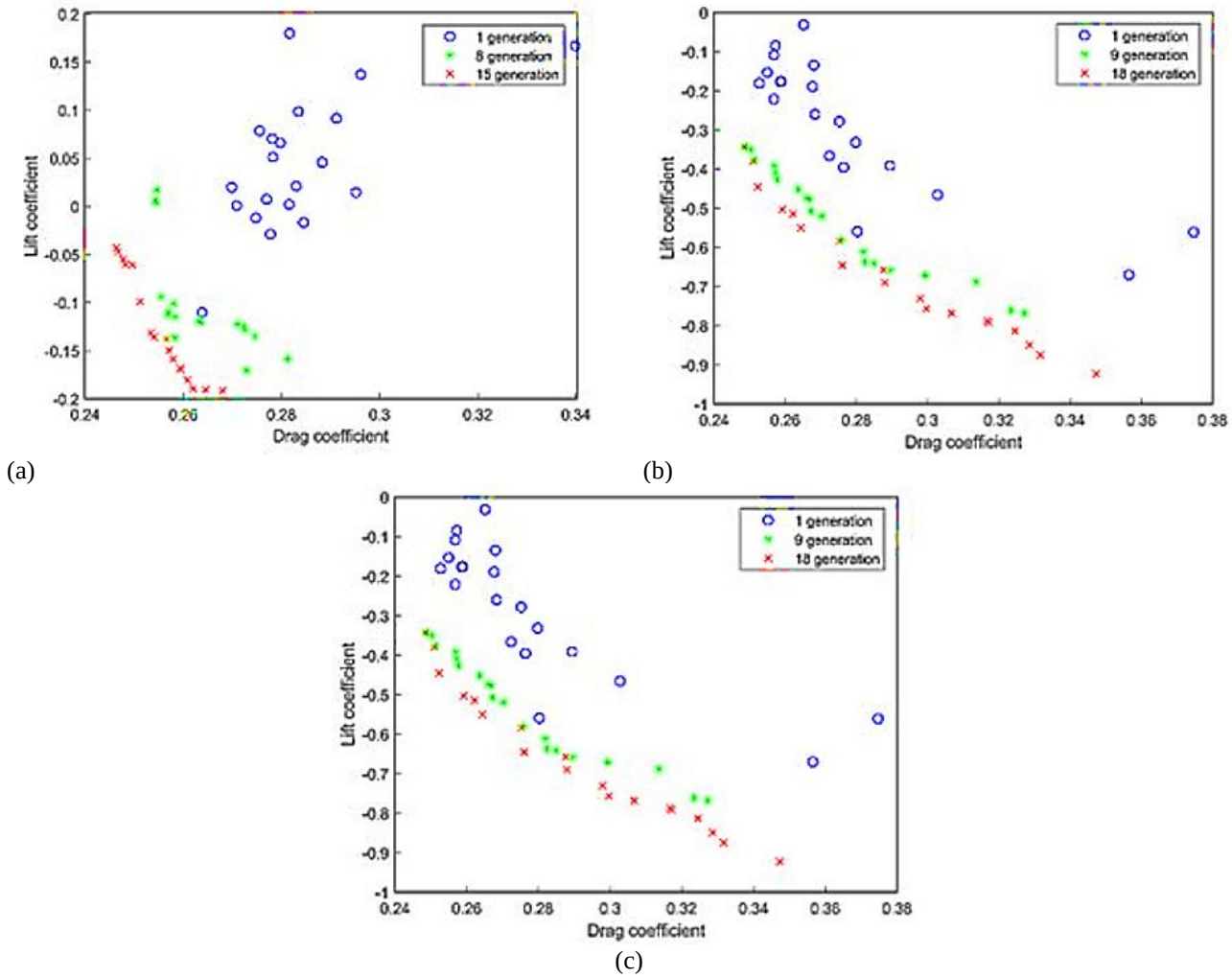

Fig. 8. Solution progressions with 3 different generations for the optimization of (a) flap-only, (b) diffuser-only, and (c) combined flap-diffuser.

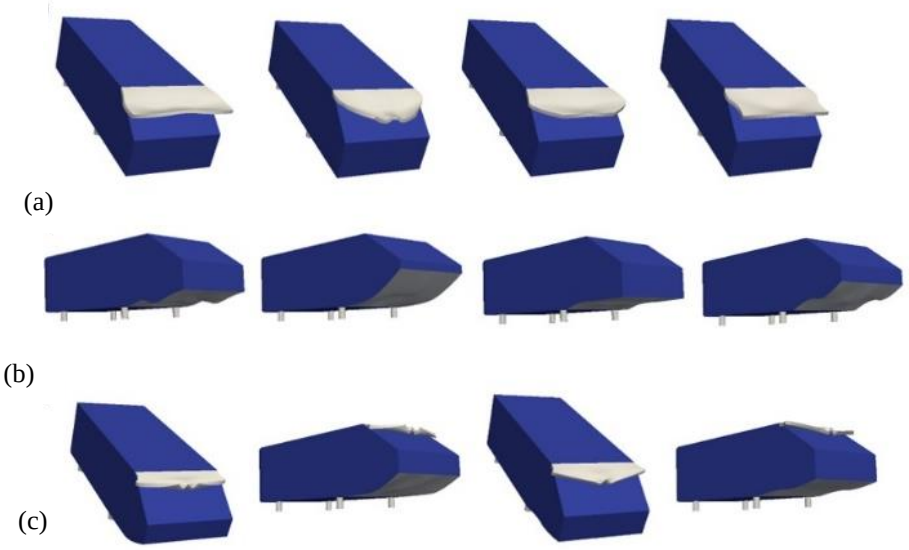

Fig. 9. Examples of rows of (a) flap-only, (b) diffuser-only, and (c) combined flaps and diffusers on the Ahmed body with a 35º slant.

Table 2 Drag and lift coefficients of baseline and three optimized models. (Lift is in the Z direction)

Coefficient	Base model	Flap-only	Diffuser-only	Combined
C_d	0.2629	0.2464	0.2486	0.2435
C_l	0.0082	-0.0430	-0.3961	-0.3686

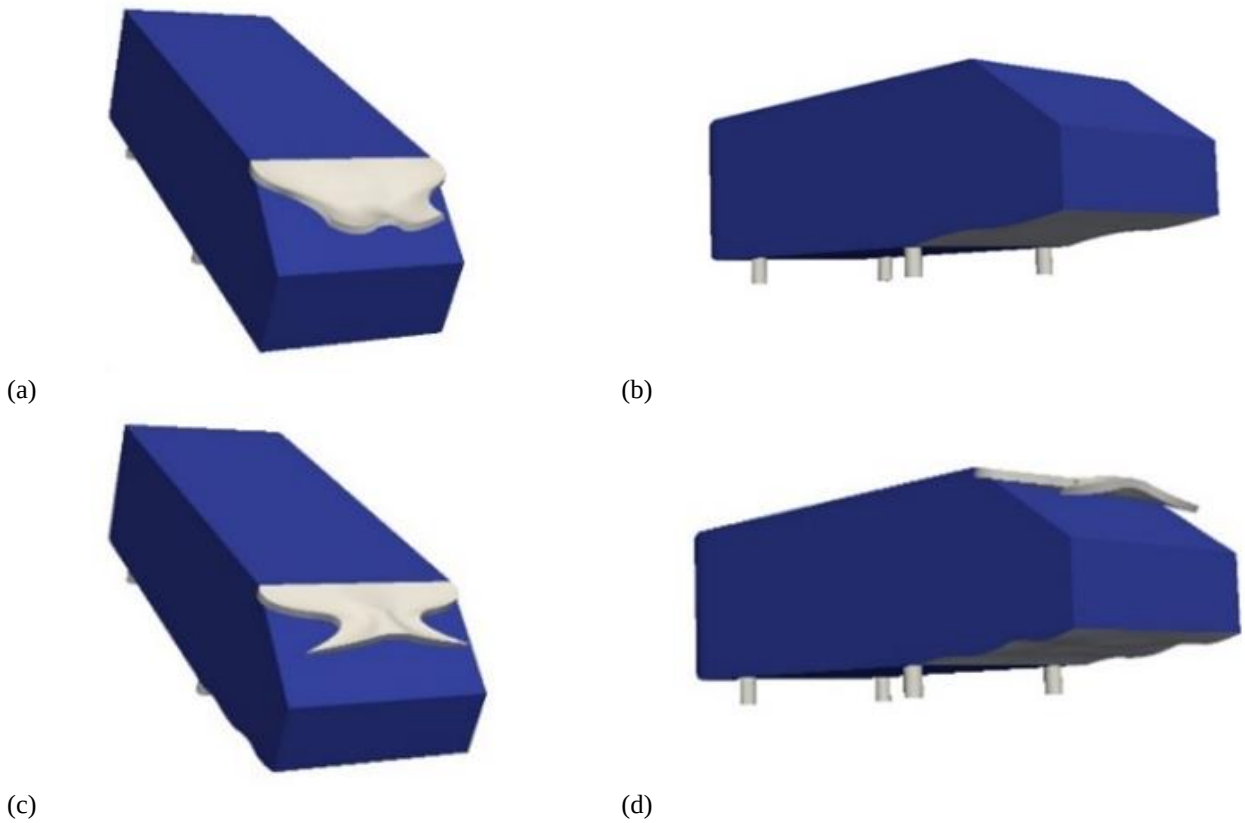

Fig. 10. Selected geometries for detailed analyses from the optimization cases of (a) flap-only, (b) diffuser-only, and (c)-(d) combined flap-diffuser in two orientations.

Also, the lower pressure region shifted further away from the Ahmed body with the flap-only case, justifying the drag reduction. In addition, a high pressure region is observed at the top of the flap, which implies there is downforce, whereas the baseline model is only evident with lift forces. The presence of an optimized flap-only resulted in 6.3% DR and 624.4% increase in downforce relative to the baseline case. For the diffuser-only model, the ground effect can be observed where there is a decrease in pressure under the vehicle body up to the neck of the diffuser, providing significant downforce. A similar behavior was not observed in both the baseline or flap-only cases. In addition, the diffuser allows pressure recovery at the rear of the Ahmed body, as evident by the pressure behind the vehicle when compared with the baseline model, resulting in DR. Overall, the selected diffuser-only model reduced the drag coefficient by 5.4% and increased downforce by 4930.5% relative to the baseline model. Since the baseline model has a lift coefficient close to zero, it explains the large improvement in the lift reduction.

By using the NSGA-II as an optimization method, it was possible to capture the benefits from both flap and diffuser devices at the same time. The combined flap-diffuser model showed improvements in both drag and lift reductions by 7.4% and 4595.1%, respectively, relative to the baseline model. It was also observed that the flap geometry in the combined case is less aggressive than in the flap-only case. Since drag and lift are optimized simultaneously, the flap-only case requires a concave shape on the flap to generate adequate downforces. However, downforce can be achieved with a diffuser in the combined case such that the flap results in a slightly convex shape to delay flow separation and promote pressure recovery and DR. Among the three selected optimized conditions, the combined flap-diffuser case resulted in the best pressure recovery, which was evident from the highest pressure behind the vehicle body, especially in the region under the flap; thus, the combined model had the lowest drag coefficient. Furthermore, the convex bumps at the end of the diffuser provided extra downforce at the tail of the vehicle that was not seen in the diffuser-only case.

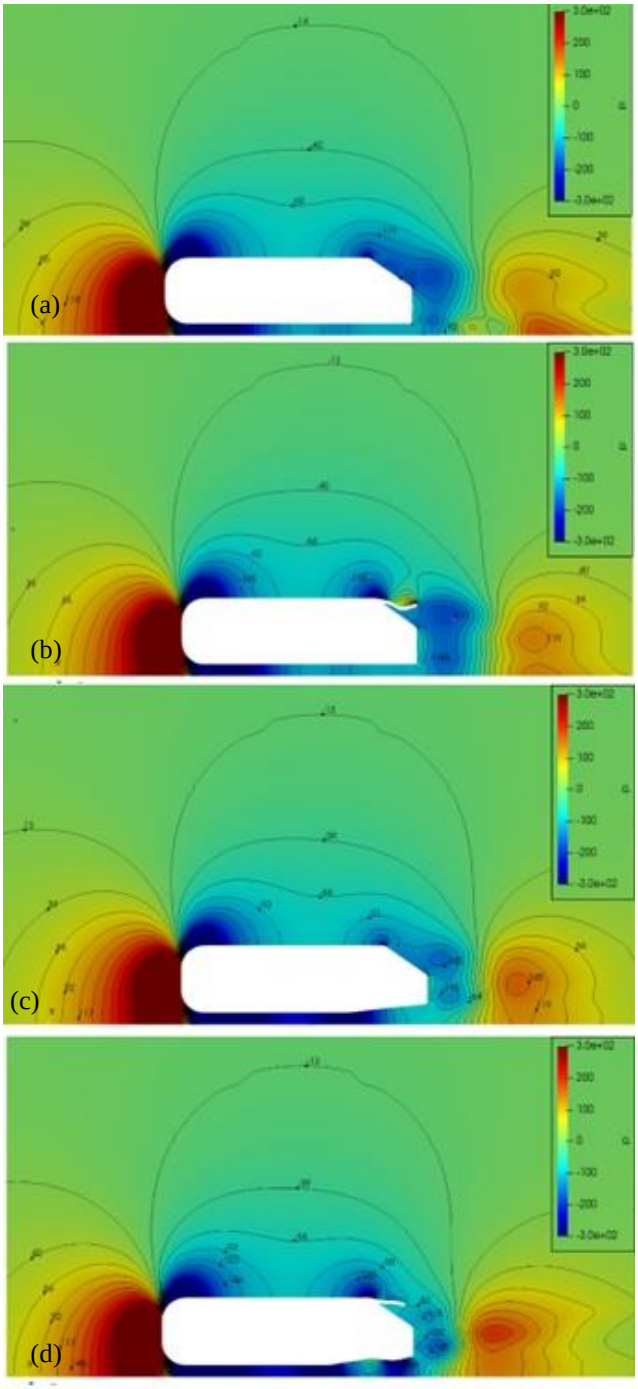

Fig. 11. Pressure contours for (a) baseline model, (b) optimized flap-only model, (c) optimized diffuser-only model, and (d) combined optimized flap-diffuser model.

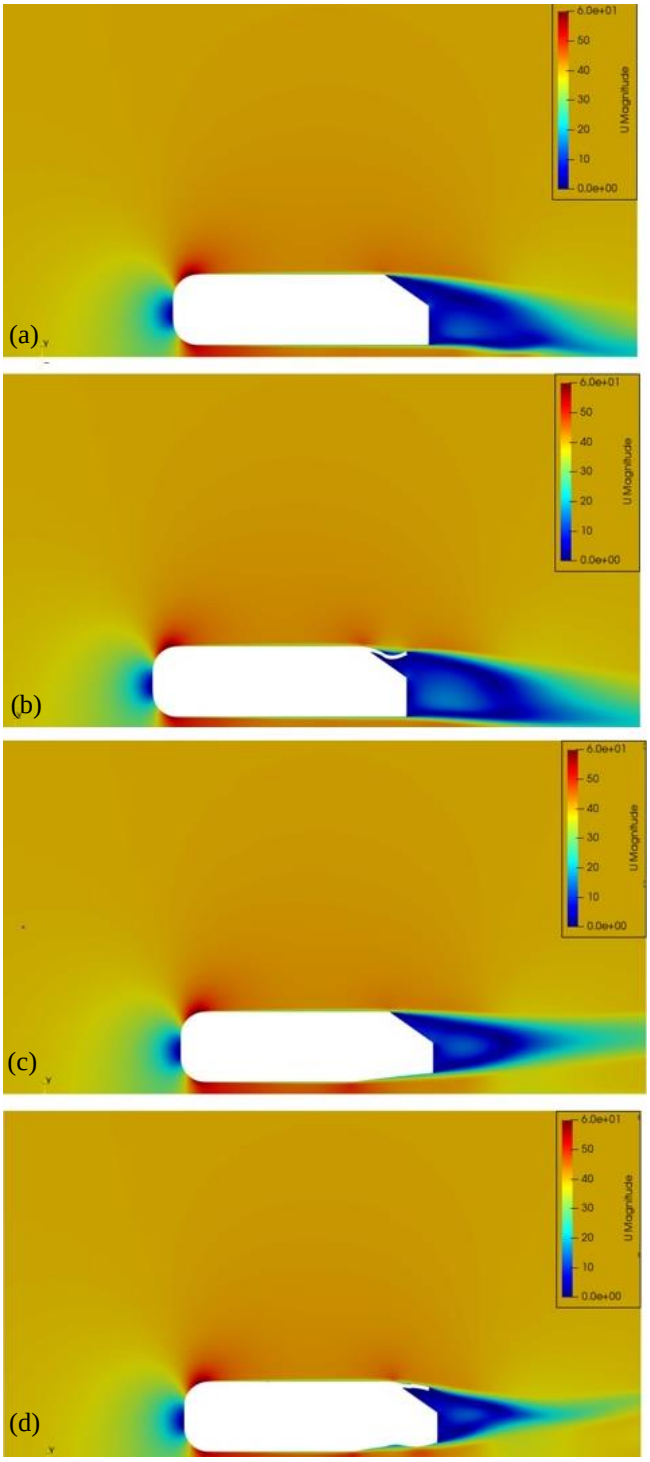

Fig. 12. Velocity profiles for (a) baseline model, (b) optimized flap-only model, (c) optimized diffuser-only model, and (d) combined optimized flap-diffuser model.

5.5 Velocity Analysis

Velocity profiles around the Ahmed body were used to visualize the overall wake region. Figure 12 shows the velocity magnitude contours defined by $U_{magnitude} = \sqrt{u^2 + v^2 + w^2}$, where u, v, w are the mean velocity components in x, y, z directions, respectively. The velocity behaviors in all the cases are consistent with the physics of the pressure contours shown previously. All the optimized flaps and diffusers were effective in creating more flow attachment to the Ahmed body, which can constrain the recirculation size and is beneficial to DR.

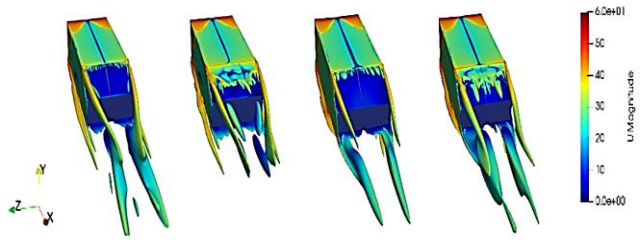

Fig. 13. Contour plots for vorticity ω_x = 200 r/s on *x*-component from left to right as: baseline, optimized flap-only, optimized diffuser-only, and combined optimized flap-diffuser models.

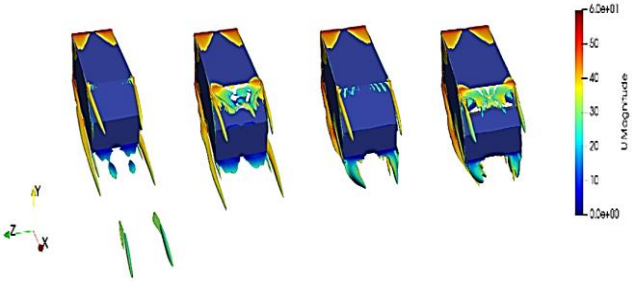

Fig. 14. Contour plots for helicity H = 7500m/s^2 from left to right: baseline, optimized flap-only, optimized diffuser-only, and combined optimized flap-diffuser models.

The recirculation size for the flap-only case was similar to that of the baseline model; therefore, the drag benefit was minimal among the other cases. Thus, the higher DR in the flap-only model can be associated with the increased vortex formation length even if the overall size of the recirculation region does not change. In contrast, the diffuser-only model shows a high drag (Table 2) by reducing the wake recirculation region since the reduction in the recirculation size is associated with the increased drag (Zdravkovich, 1981).

The Ahmed body is a three-dimensional bluff body, the pressure drag is dominant, and the addition of these devices does not much affect the contribution of skin friction drag compared to the overall pressure drag. Yet an additional surface of the flap might contribute a little higher skin friction than the diffuser, but these are insignificant.

This result was consistent with Moghimi's diffuser with a similar shape reported by Moghimi and Rafee (2018), where the least drag model is the one with the largest angle and least flow separation. The situation was further improved in the combined flap-diffuser model, which resulted in the smallest and shortest wake region. Free stream velocities were recovered sooner than all the other cases behind the vehicle; therefore, this optimized case had the least drag among all the models.

In the baseline and flap-only models, the airflow slowed down as the air moved toward the rear of the flap. Therefore, there was more pressure on the upper region, which resulted in more downforce. When a diffuser was present, the airflow was accelerated, creating a lower-pressure region under the vehicle, thus inducing downforce. In the combined flap-diffuser model, a secondary underbody flow acceleration was observed due to the convex bump shape at the end of the diffuser, which is believed to produce additional rear stability for the vehicle. The combined case was about 7% higher in the lift coefficient than the diffuser-only case, which was due to the slight flow acceleration on the top of the flap, causing pressure to reduce and explaining the underperformance of the combined case in the downforce optimization.

5.6 Vortex Identification

Further analyses were performed with vortex identification methods to provide more insights. In this section, vortices were analyzed using vorticity, helicity, Q-criterion, and spanwise (y-z) velocity magnitude. The primary factors contributing to drag increase in ground vehicles are the size of the recirculation zone and longitudinal vortices (Aider et al., 2010). Additionally, longitudinal forces also contribute to an increase in undesirable lift forces (Delassaux et al., 2021).Because both recirculation zone and longitudinal vortices have a direct influence on drag, reducing at least one of them can result in DR.

Vorticity and helicity of the baseline, flap-only, diffuser-only, and combined flap-diffuser models are shown in Fig. 13, and Fig. 14, respectively, and the longitudinal vortices were compared among the four cases. The vortices in the baseline model were the strongest compared to the optimized models. The top and bottom vortices in the baseline model merged together and then diverged as they moved away from the Ahmed body, which would enlarge and extend the wake region when they interact with the surrounding airflow. The presence of a flap device created small vortices on top of the flap and two additional vortices at the center height, but the two vortices at the bottom were reduced significantly, which contributed to DR, as shown in Fig. 13(a)-(b). In the diffuser-only case, the C-pillar vortices and bottom vortices were separated, and the bottom vortices were also straightened out, as seen in Fig. 13(c) and resulting in a smaller wake region. In the combined flap-diffuser case, the vortices on top of the flap were more directional than in the flap-only case, and the bottom ones also tapered down from stronger to weaker vortices, which resulted in the smallest recirculation behind the vehicle. The nature of flow separation differs between the flap and the diffuser. It has been highlighted by Siddiqui and Agelin-Chaab (2021) that the addition of a flap over the slant surface delayed the flow separation and increased the recirculation length in the wake. Similarly, in the current study, the addition of a flap shows a

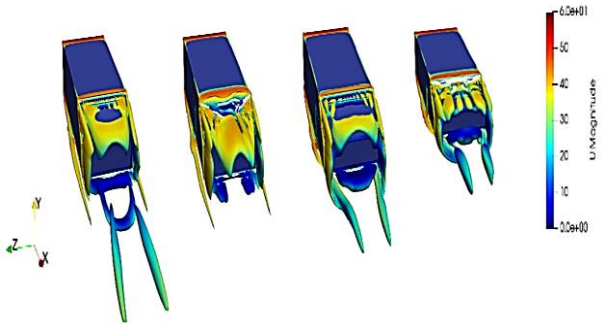

Fig. 15. Contour plots for *Q*-criterion Q/U_{ref} = 150 from left to right: baseline, optimized flap-only, optimized diffuser-only, and combined optimized flap-diffuser models, where U_{ref} is the inlet velocity.

delay in the flow separation depending on the flap shape and length. On the other hand, the diffuser is influenced by the flow separation at the rear edge of the underbody due to the formation of side edge vortices, as highlighted in Fig. 13 and Fig. 14. The flow separation impacts the strength of the vortices formed in the wake which is associated with the downforce.

The helical motion of the vortices in the baseline model extended until the end of the wake region, which was eliminated in the models with optimized devices. The longitudinal vortices underneath the body are known to affect not only drag but lift as well. It was observed that the downforce enhancement is due to the existence of the side edge vortices coming out of the underbody surface. The edge vortices are highly concentrated with a high axial speed core and high vorticity levels (George & Donis, 1983; Zhang et al., 2004). The turbulence levels at the core are low, and the vortices are stable, as shown in Fig. 14, It should be noted that even though longitudinal vortices are mostly undesirable, the presence of these vortices does not necessarily increase the drag as long as the flow is still attached to the vehicle, which was observed in the present study and others (George & Donis, 1983; Zhang et al., 2004). The optimized diffusers were also effective in eliminating the longitudinal vortices coming from the sides at the lower portion of the vehicle.

Figure 15 shows the contours of the *Q*-criterion vortex identification method. The contours are regions with high rotational movements that are larger than the stretching strain rates. It can be observed that the longitudinal vortices on the optimized flap-only model dissipated quicker and were shorter, while the vortices in the baseline model extended until the end of the wake region. In the optimized diffuser model, stronger vortices underneath the Ahmed body were formed, while the vortices at the upper region were weakened due to the presence of the diffuser. The combined flap-diffuser case suggested the best flow attachment among the four different conditions, allowing better pressure recovery. The upper longitudinal vortices were reduced compared to the flap-only case for more DR, and the bottom vortices were strengthened to extend to the end of the wake region for higher downforce generation.

The combined optimization strategy for the flap and diffuser was shown to be promising, as the model could capture the necessary features to reduce drag and lift while maintaining the balance between the benefits that the two devices brought as compared to flap-only or diffuser-only optimizations. The results of the combined case showed similar performances with respect to the models with individual devices. The combined optimization had to take care of 30-dimensional variables, whereas the individual optimization only consisted of less than 18 design variables. Therefore, it is believed that the combined case requires more computational time for the best results.

6. CONCLUSION

This paper proposed an intelligent passive device generator (IPDG) for the generation of unconventional and unique shapes of passive flow control (PFC) devices. The IPDG involves the integration of genetic algorithms, B-spline surfaces, and CFD. The genetic algorithm employed is elitist, so it passes on the best traits to the later generations. To demonstrate the method, PFC devices, such as rear flaps and underbody diffusers, were designed and optimized for road vehicles. The optimization ran up to 15-18 generations with a population size of 20. Three optimization scenarios were considered, including flap-only, diffuser-only, and combined flap-diffuser, using the generic Ahmed body with a 35° slant angle. The proposed method was effective in finding unique geometries that reduced drag and lift simultaneously. The following conclusions can be drawn from the study:

- The proposed IPDG demonstrated the ability to generate unique and non-intuitive device geometries, which are difficult for a human designer to conceptualize. The method was successful in optimizing multiple objectives simultaneously, which eliminated the need for parametric studies that could be laborious.
- The flap reduced drag by promoting flow attachment and also produced downforce. The flap-only case had a concave shape such that airflow was slowed down and pressure was increased on top of the flap. It successfully reduced drag by 6.3% and increased downforce by 624.4% compared with the baseline model without devices. The presence of the flap also affected the recirculation zone such that there was more attached airflow and weaker longitudinal
- The optimized diffuser-only case was effective in creating a lower-pressure region underneath the vehicle body by accelerating the airflow and increasing downforce. Higher pressure recovery was achieved when compared to the baseline

model without devices. The optimized diffuser-only case resulted in a DR of 5.4% and an increase in downforce by 4930% compared with the baseline model without devices.

- The combined flap-diffuser case has a flare at the end of the flap that weakened the vortices, whereas the diffuser has convex bumps at its end that increased the pressure to provide additional downforce at the base of the vehicle. The combined optimized flap-diffuser case reduced drag by 7.4% and improved downforce by 4595.1% compared with the baseline model without devices. However, the downforce has decreased relative to the diffuser-only case, which demonstrates that more devices do not necessarily produce the desired effect.

The proposed IPDG has great potential for the optimization of add-on aerodynamic devices for road vehicles. It also has the potential to be a universal PFC device generator that can be applied to any vehicle to improve aerodynamic performance. However, the downside of the technique is that it is computationally expensive. In future, further improvements will be made to the technique and applied to a more realistic vehicle, such as the DrivAer model.

ACKNOWLEDGEMENTS

The authors would like to acknowledge the financial support from the Natural Science and Engineering Research Council of Canada (Grant #: RGPIN-2018-05369).

AVAILABILITY OF DATA AND MATERIALS

The datasets used and/or analyzed during the current study are available from the corresponding author upon reasonable request.

CONFLICT OF INTEREST

The authors declare that they have no competing interests.

AUTHOR CONTRIBUTION

R. Aranha: Conceptualization; Data collection; Visualization; Writing the original draft. N.A. Siddiqui: Conceptualization (supporting); writing; review and editing. W.Y. Pao: Writing original draft (Supporting), review and editing. M. Agelin-Chaab: Supervision, review and editing.

REFERENCES

Ahmed, S. R., Ramm, G., & Faltin, G. (1984). Some salient features of the time-averaged ground vehicle wake. *SAE Transactions*, 93(2), 473–503. https://doi.org/10.4271/840300

Aider, J. L., Beaudoin, J. F., & Wesfreid, J. E. (2010). Drag and lift reduction of a 3D bluff-body using active vortex generators. *Experiments in Fluids*, 48(5), 771–789. https://doi.org/10.1007/s00348-009-0770-y

ANSYS, I. (2018). ANSYS User's Guide.

Banzhaf, W., Nordin, P., Keller, R. E., & Francone, F. D. (1998). Genetic programming. An introduction on the automatic evolution of computer programs and its applications. *Morgan Kaufmann Publishers Inc.*

Beaudoin, J. F., & Aider, J. L. (2008). Drag and lift reduction of a 3D bluff body using flaps. *Experiments in Fluids*, 44(4), 491–501. https://doi.org/10.1007/s00348-007-0392-1

Cornejo MacEda, G. Y., Li, Y., Lusseyran, F., Morzyński, M., & Noack, B. R. (2021). Stabilization of the fluidic pinball with gradient-enriched machine learning control. *Journal of Fluid Mechanics*, 917, A42. https://doi.org/10.1017/jfm.2021.301

Cornejo Maceda, G. Y., Noack, B. R., Lusseyran, F., Deng, N., Pastur, L., & Morzynski, M. (2019). Artificial intelligence control applied to drag reduction of the fluidic pinball. *PAMM*, 19(1), e201900268. https://doi.org/10.1002/pamm.201900268

Deb, K., Pratap, A., Agarwal, S., & Meyarivan, T. (2002). A fast and elitist multiobjective genetic algorithm: NSGA-II. *IEEE Transactions on Evolutionary Computation*, 6(2), 182-197. https://doi.org/10.1109/4235.996017

Delassaux, F., Mortazavi, I., Itam, E., Herbert, V., & Ribes, C. (2021). Sensitivity analysis of hybrid methods for the flow around the Ahmed body with application to passive control with rounded edges. *Computers and Fluids*, 214, 104757. https://doi.org/10.1016/j.compfluid.2020.104757

Doyle, J. B., Hartfield, R. J., & Roy, C. (2008). *Aerodynamic optimization for freight trucks using a genetic algorithm and CFD*. 46th AIAA Aerospace Sciences Meeting and Exhibit (p.323). https://doi.org/10.2514/6.2008-323

Duriez, T., Brunton, S. L., & Noack, B. R. (2013). *Machine learning dynamics and taming nonlinear control – turbulence*. Springer. https://doi.org/10.1007/978-3-319-40624-4

Fan, D., Zhang, B., Zhou, Y., & Noack, B. R. (2020). Optimization and sensitivity analysis of active drag reduction of a square-back Ahmed body using machine learning control. *Physics of Fluids*, 32(12), 125117. https://doi.org/10.1063/5.0033156

Fourrié, G., Keirsbulck, L., Labraga, L., & Gilliéron, P. (2011). Bluff-body drag reduction using a deflector.

Experiments in Fluids, 50(2), 385–395. https://doi.org/10.1007/s00348-010-0937-6

Gautier, N., Aider, J. L., Duriez, T., Noack, B. R., Segond, M., & Abel, M. (2015). Closed-loop separation control using machine learning. *Journal of Fluid Mechanics*, 770, 442-457. https://doi.org/10.1017/jfm.2015.95

George, A. R., & Donis, J. E. (1983, November 13-18). *Flow patterns, pressures, and forces on the underside of idealized ground effect vehicles.* Aerodynamics of Transportation-ii, ASME Winter Annual Meeting, Boston, USA.

Goldberg, D. E., & Holland, J. H. (1988). *Genetic algorithms and machine learning*. Machine Learning, Springer. https://doi.org/10.1023/A:1022602019183

Guilmineau, E. (2008). Computational study of flow around a simplified car body. *Journal of Wind Engineering and Industrial Aerodynamics*, 96(6–7), 1207–1217. https://doi.org/10.1016/j.jweia.2007.06.041

Hanfeng, W., Yu, Z., Chao, Z., & Xuhui, H. (2016). Aerodynamic drag reduction of an Ahmed body based on deflectors. *Journal of Wind Engineering and Industrial Aerodynamics*, 148, 34–44. https://doi.org/10.1016/j.jweia.2015.11.004

Hassanat, A., Almohammadi, K., Alkafaween, E., Abunawas, E., Hammouri, A., & Prasath, V. B. S. (2019). Choosing mutation and crossover ratios for genetic algorithms-a review with a new dynamic approach. *Information (Switzerland)*, 10(12). https://doi.org/10.3390/info10120390

Koza, J. R. (1994). Genetic programming as a means for programming computers by natural selection. *Statistics and Computing*, 4(2), 87-112. https://doi.org/10.1007/BF00175355

Lee, C., Kim, J., Babcock, D., & Goodman, R. (1997). Application of neural networks to turbulence control for drag reduction. *Physics of Fluids*, 9(6), 1740-1747. https://doi.org/10.1063/1.869290

Li, R., Noack, B. R., Cordier, L., Borée, J., & Harambat, F. (2017). Drag reduction of a car model by linear genetic programming control. *Experiments in Fluids*, 58(8), 1–20. https://doi.org/10.1007/s00348-017-2382-2

Li, Y., Cui, W., Jia, Q., Li, Q., Yang, Z., Morzyński, M., & Noack, B. R. (2022). Explorative gradient method for active drag reduction of the fluidic pinball and slanted Ahmed body. *Journal of Fluid Mechanics*, 932, A7. https://doi.org/10.1017/jfm.2021.974

Lienhart, H., Stoots, C., & Becker, S. (2002). *Flow and turbulence structures in the wake of a simplified car model (Ahmed Modell).* New Results in Numerical and Experimental Fluid Mechanics III, Springer Berlin Heidelberg. https://doi.org/10.1007/978-3-540-45466-3_39

Liu, C., Bu, W., & Xu, D. (2017). Multi-objective shape optimization of a plate-fin heat exchanger using CFD and multi-objective genetic algorithm. *International Journal of Heat and Mass Transfer*, 111, 65-22. https://doi.org/10.1016/j.ijheatmasstransfer.2017.03.066

Meile, W., Brenn, G., Reppenhagen, A., Lechner, B., & Fuchs, A. (2012). Experiments and numerical simulations on the aerodynamics of the Ahmed body. *CFD letters*, 3(1), 32-39.

Moghimi, P., & Rafee, R. (2018). Numerical and experimental investigations on aerodynamic behavior of the Ahmed body model with different diffuser angles. *Journal of Applied Fluid Mechanics*, 11(4),1101-1113. https://doi.org/10.29252/JAFM.11.04.27923

Muñoz-Paniagua, J., & García, J. (2020). Aerodynamic drag optimization of a high-speed train. *Journal of Wind Engineering and Industrial Aerodynamics*, 204, 104215. https://doi.org/10.1016/j.jweia.2020.104215

Muyl, F., Dumas, L., & Herbert, V. (2004). Hybrid method for aerodynamic shape optimization in automotive industry. *Computers and Fluids*, 33(5–6). https://doi.org/10.1016/j.compfluid.2003.06.007

Nelder, J. A., & Mead, R. (1965). A Simplex Method for Function Minimization. *The Computer Journal*, 7(4). https://doi.org/10.1093/comjnl/7.4.308

Noack, B. R. (2019). Closed-loop turbulence control-from human to machine learning (And retour). *Lecture Notes in Mechanical Engineering*, 23–32. https://doi.org/10.1007/978-981-10-7542-1_3

Patrikalakis, N. M., & Maekawa, T. (2010). *Shape interrogation for computer aided design and manufacturing*. Shape Interrogation for Computer Aided Design and Manufacturing Heidelberg, Springer. https://doi.org/10.1007/978-3-642-04074-0

Raibaudo, C., Zhong, P., Noack, B. R., & Martinuzzi, R. J. (2020). Machine learning strategies applied to the control of a fluidic pinball. *Physics of Fluids*, 32(1), 015108. https://doi.org/10.1063/1.5127202

Ren, F., Wang, C., & Tang, H. (2019). Active control of vortex-induced vibration of a circular cylinder using machine learning. *Physics of Fluids*, 31(9), 093601. https://doi.org/10.1063/1.5115258

Ren, K., Chen, Y., Gao, C., & Zhang, W. (2020). Adaptive control of transonic buffet flows over an airfoil. *Physics of Fluids*, 32(9),096106. https://doi.org/10.1063/5.0020496

Siddiqui, N. A., & Agelin-Chaab, M. (2021). A simple passive device for the drag reduction of an Ahmed body. *Journal of Applied Fluid Mechanics*, 14(1), 147–164. https://doi.org/10.47176/JAFM.14.01.31791

Tian, J., Zhang, Y., Zhu, H., & Xiao, H. (2017). Aerodynamic drag reduction and flow control of Ahmed body with flaps. *Advances in Mechanical Engineering*, 9(7), 1–17. https://doi.org/10.1177/1687814017711390

Wu, Z., Fan, D., Zhou, Y., Li, R., & Noack, B. R. (2018). Jet mixing optimization using machine learning control. *Experiments in Fluids*, 59(8), 1-17. https://doi.org/10.48550/arXiv.1802.01252

Yang, X. S. (2013). Optimization and metaheuristic algorithms in engineering. *Metaheuristics in Water, Geotechnical and Transport Engineering*,1, 23. https://doi.org/10.1016/B978-0-12-398296-4.00001-5

Yu, M. G., Zhang, J. Y., & Zhang, W. H. (2013). Multi-objective optimization design method of the high-speed train head. *Journal of Zhejiang University: Science A*, 14(9). https://doi.org/10.1631/jzus.A1300109

Yu, Z., & Bingfu, Z. (2021). Recent advances in wake dynamics and active drag reduction of simple automotive bodies. *Applied Mechanics Reviews*, 73(6), 060801. https://doi.org/10.1115/1.4053132

Yuan, C. Y., & Li, M. Q. (2017). Multi-objective optimization for the aerodynamic noise of the high-speed train in the near and far field based on the improved NSGA-II algorithm. *Journal of Vibroengineering*, 19(6), 4759–4782. https://doi.org/10.21595/jve.2017.18526

Zdravkovich, M. M. (1981). Review and classification of various aerodynamic and hydrodynamic means for suppressing vortex shedding. *Journal of Wind Engineering and Industrial Aerodynamics*, 7(2), 145–189. https://doi.org/10.1016/0167-6105(81)90036-2

Zhang, X., Senior, A., & Ruhrmann, A. (2004). Vortices behind a bluff body with an upswept aft section in ground effect. *International Journal of Heat and Fluid Flow*, 25(1),1-9. https://doi.org/10.1016/j.ijheatfluidflow.2003.11.002

Zhou, Y., Zhou, Y., Fan, D., Zhang, B., Li, R., Li, R., Noack, B. R., Noack, B. R., & Noack, B. R. (2020). Artificial intelligence control of a turbulent jet. *Journal of Fluid Mechanics*, 897, *A27*. https://doi.org/10.1017/jfm.2020.392